

## PHYSICS

# Critical behavior within 20 fs drives the out-of-equilibrium laser-induced magnetic phase transition in nickel

Phoebe Tengdin,<sup>1\*</sup> Wenjing You,<sup>1\*</sup> Cong Chen,<sup>1</sup> Xun Shi,<sup>1†</sup> Dmitriy Zusin,<sup>1</sup> Yingchao Zhang,<sup>1</sup> Christian Gentry,<sup>1</sup> Adam Blonsky,<sup>1</sup> Mark Keller,<sup>2</sup> Peter M. Oppeneer,<sup>3</sup> Henry C. Kapteyn,<sup>1</sup> Zhensheng Tao,<sup>1†</sup> Margaret M. Murnane<sup>1</sup>

It has long been known that ferromagnets undergo a phase transition from ferromagnetic to paramagnetic at the Curie temperature, associated with critical phenomena such as a divergence in the heat capacity. A ferromagnet can also be transiently demagnetized by heating it with an ultrafast laser pulse. However, to date, the connection between out-of-equilibrium and equilibrium phase transitions, or how fast the out-of-equilibrium phase transitions can proceed, was not known. By combining time- and angle-resolved photoemission with time-resolved transverse magneto-optical Kerr spectroscopies, we show that the same critical behavior also governs the ultrafast magnetic phase transition in nickel. This is evidenced by several observations. First, we observe a divergence of the transient heat capacity of the electron spin system preceding material demagnetization. Second, when the electron temperature is transiently driven above the Curie temperature, we observe an extremely rapid change in the material response: The spin system absorbs sufficient energy within the first 20 fs to subsequently proceed through the phase transition, whereas demagnetization and the collapse of the exchange splitting occur on much longer, fluence-independent time scales of ~176 fs. Third, we find that the transient electron temperature alone dictates the magnetic response. Our results are important because they connect the out-of-equilibrium material behavior to the strongly coupled equilibrium behavior and uncover a new time scale in the process of ultrafast demagnetization.

## INTRODUCTION

As a ferromagnetic metal approaches the Curie temperature, it reaches a critical point where the magnetic properties of the material change dramatically. Under equilibrium conditions, this ferromagnetic-to-paramagnetic phase transition is associated with critical phenomena, characterized by a vanishing of the spontaneous magnetization as well as a divergence of the magnetic heat capacity and susceptibility (1). A faster route to change the magnetization is to use femtosecond laser irradiation: Since the first experimental observation of ultrafast laser-induced demagnetization (2), femtomagnetism has been a subject of intense experimental and theoretical studies. Although one might expect critical phenomena to play an important role in laser-induced demagnetization of ferromagnetic metals, to date, there has been no clear evidence of this.

When a ferromagnetic metal is heated with a femtosecond laser pulse, the energy is directly coupled into the electron bath, creating an out-of-equilibrium electron distribution. This electron energy distribution quickly thermalizes (within tens of femtoseconds) to a hot Fermi-Dirac energy distribution. In most past work, the laser-induced demagnetization process is described as a sequence of events where the energy of the hot electron bath transfers first to the spin and later to the lattice degrees of freedom. This cascade of energy relaxation processes is used to explain why ultrafast demagnetization occurs over a range of time scales from ~100 to 500 fs (2, 3). These multiple time scales observed in past experiments obscured any contributions from

critical phenomena. Although there is still no consensus on the important microscopic mechanisms that drive ultrafast demagnetization, or their relevant time scales, a number of microscopic models have been proposed. These are based on spin-flip scattering (3–8) that transfers spin angular momenta during the demagnetization process, as well as laser-induced polarized (9–11) or unpolarized (12, 13) spin currents that can also lead to ultrafast demagnetization.

Here, we present clear evidence that critical behavior on a new ultrafast 20-fs time scale governs laser-induced demagnetization in nickel. We show this by correlating time- and angle-resolved photoelectron spectroscopy (Tr-ARPES) with time-resolved transverse magneto-optical Kerr effect (Tr-TMOKE) spectroscopy, as well as with extreme ultraviolet (EUV) transient reflectivity, all using tabletop high-harmonic sources (14). Through fluence- and temperature-dependent studies, we make several surprising observations. First, we observe critical behavior as the spin system undergoes a transient magnetic phase transition: As the laser fluence approaches a critical fluence  $F_c$  of ~2.8 mJ/cm<sup>2</sup>, corresponding to a hot electron temperature approaching the Curie temperature (~631 K), significantly more laser energy is required to increase the peak electron temperature, indicating a divergence in the heat capacity of the spin system. Second and very surprisingly, the spin system absorbs sufficient energy within the first 20 fs to subsequently proceed through the phase transition. This defines a new time scale in the process of ultrafast demagnetization. Demagnetization (measured using TMOKE) and the collapse of the exchange splitting (measured using ARPES) both occur on much longer and similar time scales of ~176 fs, independent of the laser fluence. Third, the recovery dynamics of the exchange splitting also exhibit a critical behavior, changing from a full recovery within 500 fs when pumped at fluences below  $F_c$  to a much longer 76-ps recovery above  $F_c$ . These critical phenomena indicate that the transient electron temperature alone dictates the magnetic response.

<sup>1</sup>Department of Physics and JILA, University of Colorado and National Institute of Standards and Technology (NIST), Boulder, CO 80309, USA. <sup>2</sup>NIST, 325 Broadway, Boulder, CO 80305, USA. <sup>3</sup>Department of Physics and Astronomy, Uppsala University, Box 516, 75120 Uppsala, Sweden.

\*These authors contributed equally to this work.

†Corresponding author. Email: xun.shi@colorado.edu (X.S.); zhensheng.tao@jila.colorado.edu (Z.T.)

We note that our findings are in contrast to past work assuming that the electron bath alone absorbs the laser energy, which is then slowly transferred to the spin system throughout the demagnetization process (3, 5, 8, 15). Instead, our results imply that the ultrafast demagnetization of a ferromagnetic metal is driven by a highly nonequilibrium process that takes place within the first 20 fs, with sufficient energy transfer from the optical excitation to the spin system to subsequently proceed through the transient magnetic phase transition (see Fig. 1). This ultrafast, highly nonequilibrium process can likely be driven by superdiffusive spin currents (10, 11) or spin mixing via spin-orbit coupling (16–18). Then, demagnetization of the sample occurs on a longer time scale of  $\sim 176$  fs, likely mediated by processes such as low-energy magnon generation.

## RESULTS

The observed critical behavior in laser-induced ultrafast demagnetization in nickel is shown schematically in Fig. 1A. Our time-resolved ARPES and TMOKE measurements were both performed using 780-nm laser-driven EUV high-harmonic generation (HHG) probe beams, as shown in Fig. 1 (B and C) (see Materials and Methods). For all measurements, the sample used is a 400-nm Ni(111) single-crystalline film grown on an  $\alpha$ -Al<sub>2</sub>O<sub>3</sub>(0001) substrate (19). The Ni film thickness is much greater than both the pumping ( $\sim 13$  nm) and probing depth ( $\sim 1$  nm for ARPES;  $\sim 10$  nm for TMOKE) to avoid any influence of the substrate, capping layer, or multilayer structure (11–13, 20).

The characteristic dynamics of Ni demagnetization measured by TMOKE, as well as of the exchange splitting ( $E_{\text{ex}}$ ) measured by ARPES, are plotted in Fig. 2A as a function of pump-probe time delay ( $t_d$ ). The TMOKE asymmetry  $A_s$  (see Materials and Methods) at 360 fs before the pump pulse arrives and 500 fs after the pump pulse arrives is plotted

in Fig. 2B, where a clear reduction of the asymmetry can be observed after laser excitation. Tr-TMOKE is a momentum-averaged measurement, as shown in the Supplementary Materials. For ARPES, the photoelectron spectra along the  $\bar{\Gamma} - \bar{K}$  direction at room temperature are shown in Fig. 2C. Before the pump pulse excites the sample ( $t_d = -500$  fs), the exchange splitting ( $E_{\text{ex}}$ ) between the majority and minority bands of Ni can be observed at momentum  $k_{\parallel} \approx 1.05 \text{ \AA}^{-1}$ , where the  $d$  band crosses the Fermi energy ( $E_F$ ) (21, 22). The exchange splitting  $E_{\text{ex}}$  reduces after laser excitation, as indicated by the spectrum taken 500 fs after the pump pulse and the extracted photoemission intensity. The values of  $E_{\text{ex}}$  are obtained by fitting the extracted spectra with multiple Voigt functions (see Fig. 2C and the Supplementary Materials).

The dynamics of the exchange-splitting change ( $\Delta E_{\text{ex}}$ ) and TMOKE asymmetry ( $A_s$ ) can be generally fit by an exponential decay and bi-exponential recovery function (see Materials and Methods). We find that the dynamics of  $\Delta E_{\text{ex}}$  can be described by a set of time constants, with a dramatic change in recovery times above a critical laser fluence. For all pump laser fluences (below or above the critical fluence), the collapse of the exchange splitting exhibits a constant and fluence-independent time scale of  $176 \pm 27$  fs. For fluences below a critical laser fluence of  $F_c \approx 2.8 \text{ mJ/cm}^2$ , the magnetic response exhibits a fast recovery ( $\tau_{\text{recover1}} = 537 \pm 173$  fs). For fluences above  $F_c$ , the magnetic response exhibits the same fast recovery as well as a slower recovery ( $\tau_{\text{recover2}} = 76 \pm 15$  ps; see the Supplementary Materials). These characteristic time constants are obtained using a global fitting scheme (see the Supplementary Materials). We note that the minima of dynamics shown in Fig. 2A depend on the ratio of demagnetization and fast recovery amplitudes. Although they appear at different time delays for different fluences, the extracted time constants (and characteristic time scales of the processes) are the same. To correlate the dynamics of the

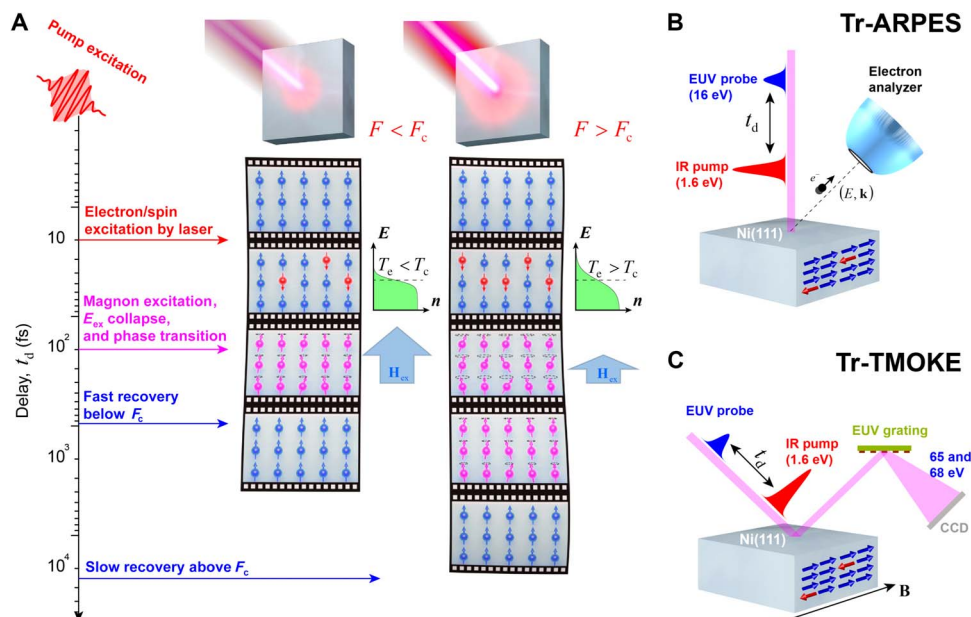


**Fig. 1. Schematic of the critical behavior of ultrafast demagnetization in Ni.** (A) After excitation by a femtosecond laser pulse above the critical fluence ( $F_c$ ), the transient electron temperature ( $T_e$ ) is driven above the Curie temperature ( $T_c$ ), inducing high-energy spin excitations within 20 fs, which store the magnetic energy (see text). The Fermi-Dirac distributions of electrons are also plotted. Demagnetization occurs later, in  $\sim 176$  fs, driven by relaxation of nonequilibrium spins and the likely excitation of low-energy magnons. Full recovery of the spin system occurs within  $\sim 500$  fs to  $\sim 76$  ps, depending on the laser fluence. (B and C) Experimental setups for time-resolved ARPES and TMOKE, respectively, using ultrafast high-harmonic sources. IR, infrared.

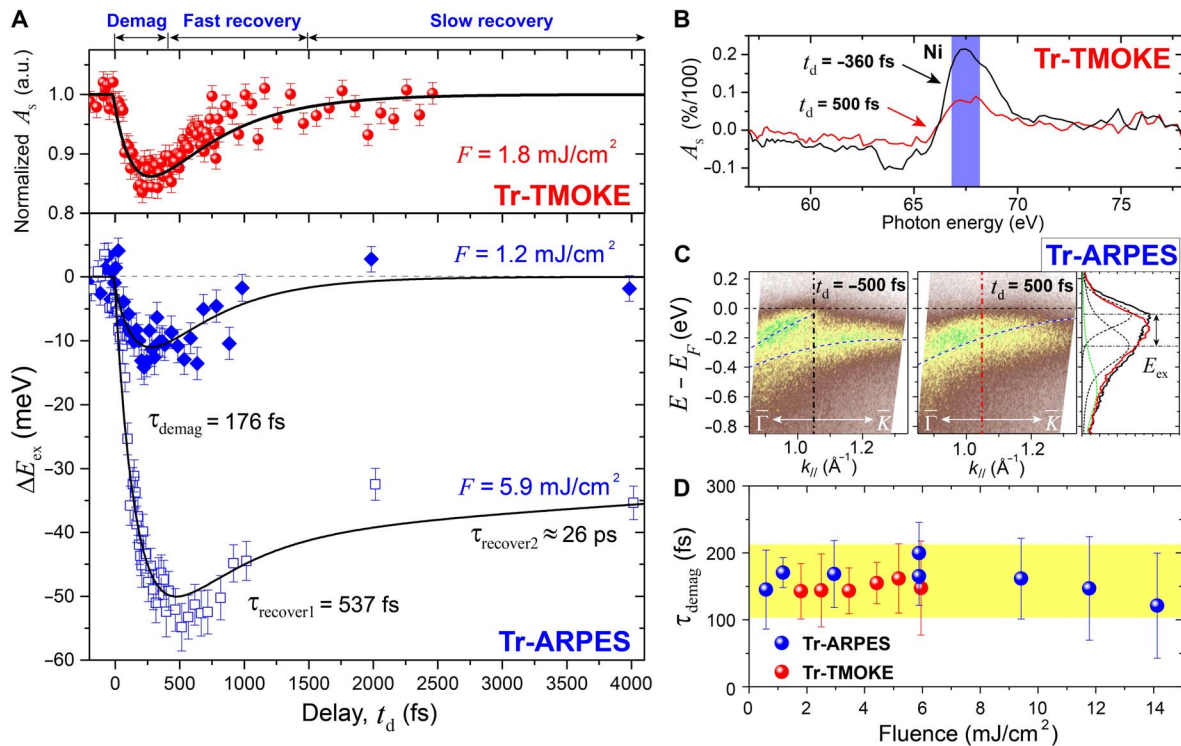


**Fig. 2. Magnetization dynamics in Ni.** (A) Change of the TMOKE asymmetry and exchange splitting reduction  $\Delta E_{\text{ex}}$  as a function of time delay for different laser fluences. The solid lines represent fitting results, from which we extract the three characteristic times for demagnetization ( $\tau_{\text{demag}}$ ), fast recovery ( $\tau_{\text{recover1}}$ ), and slow recovery ( $\tau_{\text{recover2}}$ ) (see Materials and Methods). The fit to TMOKE (upper panel) and ARPES (lower panel and lower fluence) yields the same fluence-independent time constants. a.u., arbitrary units. (B) Typical TMOKE asymmetry before ( $t_d = -360 \text{ fs}$ ) and after ( $t_d = 500 \text{ fs}$ ) laser excitation with a pump fluence  $F \approx 6 \text{ mJ/cm}^2$ . (C) Photoelectron spectra of Ni(111) along the  $\Gamma - \bar{K}$  direction before ( $t_d = -500 \text{ fs}$ ) and after ( $t_d = 500 \text{ fs}$ ) laser excitation, showing the collapse in the exchange splitting  $E_{\text{ex}}$  after excitation (blue dashed lines). The dashed-dotted lines represent the momentum at which photoemission intensities are extracted. The photoemission intensities are plotted in the right panel with  $E_{\text{ex}}$  extracted from a Voigt function fit to the data (dashed lines; see the Supplementary Materials). (D) Constant, fluence-independent demagnetization time observed for different laser fluences for both ARPES and TMOKE.

exchange-splitting collapse  $\Delta E_{\text{ex}}$  (probed by ARPES) with the laser-induced demagnetization of the sample, we analyze TMOKE measurements taken at similar pump fluences. We find that the time scale of demagnetization measured using TMOKE is the same as the exchange-splitting collapse measured using ARPES and that both are independent of the pump laser fluence (Fig. 2D). This is consistent with the conclusion that the collapse of  $E_{\text{ex}}$  obtained in Tr-ARPES directly represents the quenching of the magnetization in the material, although the dynamics are obtained at a specific momentum.

In time-resolved ARPES, the dynamic electron temperature can be directly extracted by analyzing the photoemission intensity distribution above  $E_F$ . In Fig. 3A, we plot the photoemission intensity from above  $E_F$  at different time delays, for a fluence of  $\sim 6 \text{ mJ/cm}^2$ . Before the pump pulse arrives ( $t_d = -500 \text{ fs}$ ), the photoemission intensity corresponds to a Fermi-Dirac distribution across  $E_F$  at room temperature. The electron temperature reaches its maximum value at  $\sim 24 \text{ fs}$  after the peak of the pump pulse and then rapidly decreases due to cooling to the lattice. By  $\sim 2 \text{ ps}$  after excitation, the electron temperature is close to room temperature, as evidenced by the fact that the slope of photoemission intensity as a function of energy is very close to that obtained in the ground state ( $t_d = -500 \text{ fs}$ ) (Fig. 3A). The electron temperature can be reliably extracted by fitting the photoemission intensity with the Fermi-Dirac function convolved with the experimental energy resolution (see the Supplementary Materials). The time evolution of the elec-

tron temperature after laser excitation is plotted in Fig. 3 (B and C). These results are further corroborated by the dynamics of electron population at  $\sim 0.2 \text{ eV}$  (Fig. 3B) and the transient EUV reflectivity measurements performed at similar laser fluences (Fig. 3C). These measurements probe the charge dynamics around  $E_F$  averaged over the entire Brillouin zone, by exciting the 3p core-level electrons of Ni to electronic states around  $E_F$  (see inset of Fig. 3C). The agreement between the transient electron temperatures extracted from both ARPES and EUV reflectivity measurements suggests that the measured electron dynamics across  $E_F$  are uniform throughout  $k$ -space. The short electron thermalization time in Ni is not surprising if we consider that the lifetime of photoexcited electrons at  $\sim 1.6 \text{ eV}$  above  $E_F$  is extremely short ( $\sim 1 \text{ fs}$ ) (23), indicating very strong electron-electron interactions (see the Supplementary Materials) (24).

In Fig. 4A, we plot the maximum electron temperature extracted around  $20 \text{ fs}$ , which is the characteristic time scale for the rise of the electron temperature after excitation, as a function of the laser pump fluence. Here, we observe the first critical behavior: The increase of the electron temperature is strongly suppressed around the critical fluence  $F_c \approx 2.8 \text{ mJ/cm}^2$ , indicating that a significant amount of energy is transferred into the spin system within  $\sim 20 \text{ fs}$ , preventing a further increase in electron temperature. The critical behavior of the peak electron temperature (Fig. 4A) can be explained by the divergence of the heat capacity of the strongly coupled electron and spin systems in Ni.



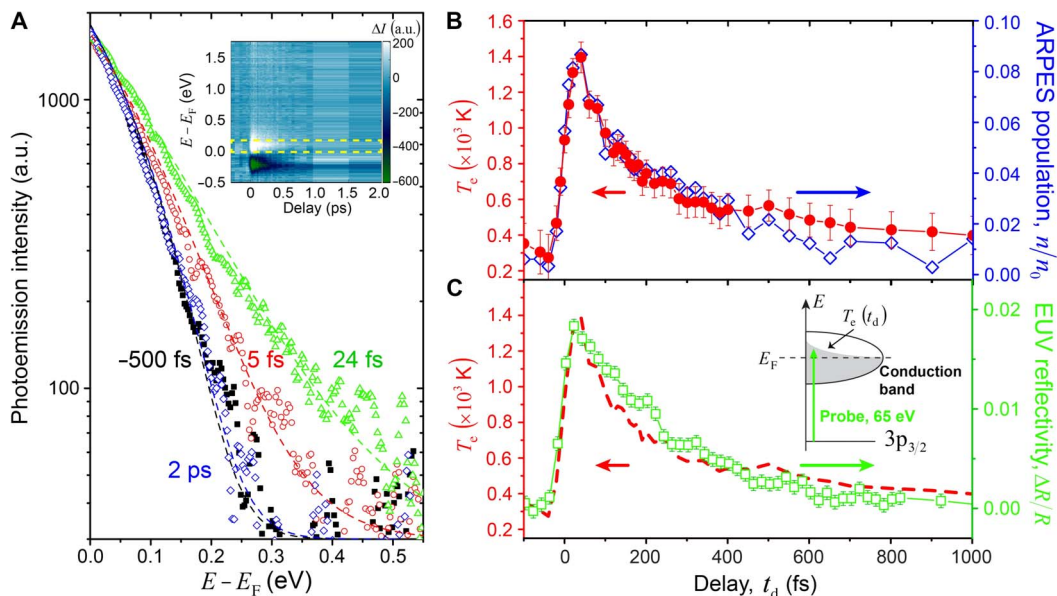


**Fig. 3. Ultrafast charge dynamics in Ni.** (A) Log plots of the photoemission intensity above  $E_F$  for  $F \approx 6$  mJ/cm<sup>2</sup> and at different  $t_d$ , integrated from  $k_{||} \approx 0.85 \text{ \AA}^{-1}$  to  $k_{||} \approx 1.3 \text{ \AA}^{-1}$  in the momentum space. The dashed lines represent the fitting of the photoemission intensities with the Fermi-Dirac distribution convolved with experimental energy resolution (see the Supplementary Materials). Inset: Integrated photoemission intensity as a function of pump-probe time delay. The yellow dashed box illustrates the integration region of electron population in (B). (B) Dynamics of the electron temperature and the relative electron population ( $n/n_0$ ) within  $\sim 0.2$  eV above  $E_F$  as a function of  $t_d$ . The electron population is normalized to the band electron population ( $n_0$ )  $\sim 0.2$  eV below  $E_F$  (see the Supplementary Materials). (C) Comparison of the electron temperature [red dashed line, same as (B)] and the change of EUV transient reflectivity at a similar pump fluence. Inset: EUV transient reflectivity measurement. The resonant EUV light (65 eV) directly probes the charge dynamics around  $E_F$  induced by the laser pump pulse. This measurement is averaged over  $k$ -space.

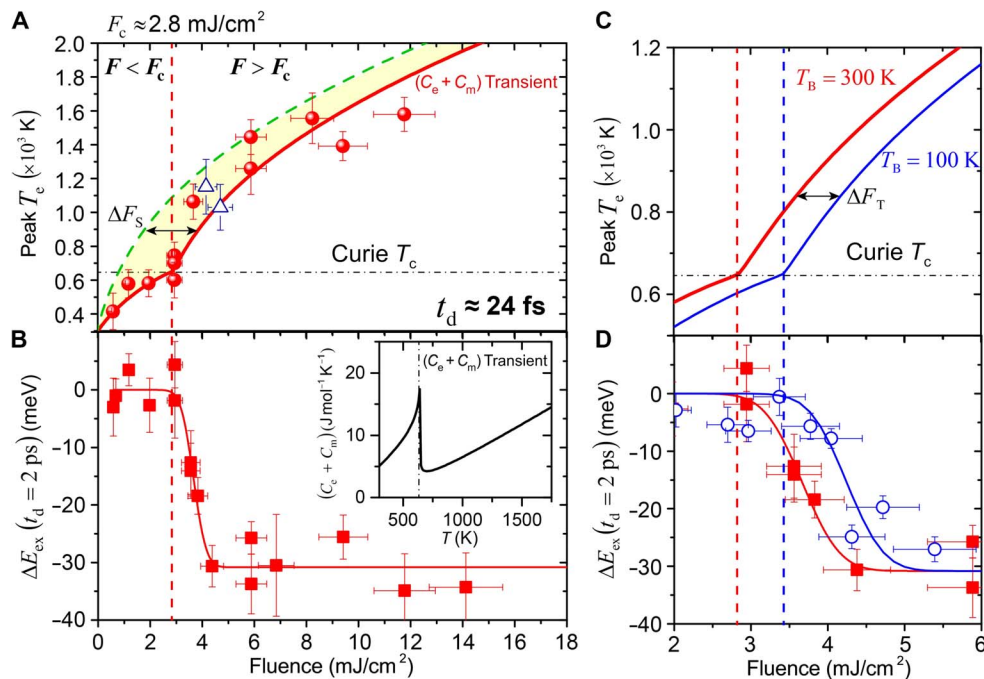


**Fig. 4. Observation of multiple critical behaviors during ultrafast demagnetization in Ni.** (A) Peak electron temperature extracted  $\sim 24$  fs after excitation as a function of pump fluence. The open symbols represent the electron temperature extracted at different  $k_{||}$  using Tr-ARPES. The solid red line is the fit using Eq. 1 considering the transient electron and magnetic heat capacity [inset of (B)], whereas the green dashed line considers only the contribution from transient electron heat capacity (see the Supplementary Materials). The yellow-colored region ( $\Delta F_S$ ) is the energy transferred to the spin system within  $\sim 20$  fs. (B) Change in the exchange splitting at 2 ps as a function of pump fluence. The red line represents a fit with an error function. The same critical fluence of  $F_c \approx 2.8$  mJ/cm<sup>2</sup> is observed for the exchange splitting collapse and the peak electron temperature in (A). The transient electron heat capacity is plotted in the inset. (C) Peak electron temperature calculated using Eq. 1 and  $(C_e + C_m)$  Transient [inset of (B)] for the sample temperatures of 300 and 100 K. The red solid line is the same as in (A). (D) Change of exchange splitting at 2 ps as a function of laser fluence at different sample temperatures. The solid lines represent the error function fit of the experimental results. The dashed lines align the critical fluences observed in (C) and (D) for different sample temperatures.

To a first-order approximation, the maximum temperature that the electrons can reach ( $T_e^{\max}$ ) at the sample surface with a given pump fluence ( $F$ ) can be calculated as

$$\frac{F(1-R)}{\delta} = \int_{T_B}^{T_e^{\max}} [C_e(T) + C_m(T)] dT \quad (1)$$

where  $R$  is the reflectivity,  $\delta$  is the penetration depth,  $T_B$  is the ground-state sample temperature, and  $C_e$  and  $C_m$  are the heat capacities of the electron and spin systems of Ni, respectively. It is well known that the magnetic heat capacity  $C_m$  diverges when the temperature approaches the Curie temperature to fulfill the energy required for the ferromagnetic-to-paramagnetic phase transitions under thermal equilibrium conditions (1, 25). Here, we model  $C_e(T) + C_m(T)$  using a power-law function and fit the measured peak electron temperature as a function of pump fluence to Eq. 1 (see Materials and Methods and the Supplementary Materials). The fitting results are shown as the solid line in Fig. 4A, which essentially captures the critical behavior of the peak electron temperature observed in our experiments. The parameters for the optimum fitting are listed in Table 1, whereas the corresponding “transient” heat capacity is plotted in the inset of Fig. 4B. We find that the divergence in the heat capacity around the critical temperature ( $T_c$ ) can quantitatively explain the critical behavior observed in the electron temperature.  $T_c$  obtained for the ultrafast transient phase transition is very close to the Curie temperature (see Table 1), which further corroborates that the critical phenomena we observed are related to the intrinsic magnetic properties of Ni. The peak electron temperatures with the contribution of electron heat capacity alone are plotted as the dashed line in Fig. 4A (see Materials and Methods and the Supplementary Materials). We estimate that there is an energy of  $\Delta E_S = \frac{\Delta F_S(1-R)}{\delta} \approx 105$  meV per unit cell transferred to the spin bath within  $\sim 20$  fs. This energy is enough to go through the magnetic phase transition because it is even higher than the energy required under thermal equilibrium conditions ( $\sim 68$  meV per unit cell) (25).

As noted above, the slow recovery of the magnetization is only observed when the pump fluence is higher than the same critical fluence  $F_c \approx 2.8$  mJ/cm<sup>2</sup>, which represents the second critical behavior. This can be illustrated if we plot the exchange-splitting collapse  $\Delta E_{\text{ex}}$  at  $t_d = 2$  ps as a function of pump laser fluence, as shown in Fig. 4B. We note that the observed critical fluence here is consistent with that shown in Fig. 4A for the electron temperature, corroborating that the observed critical behavior of the transient electron temperature is related to the laser-induced magnetic phase transition in the spin-electron system. Considering that the electron and lattice temperatures are both less than the Curie temperature of Ni at  $t_d = 2$  ps (see below), our results indicate that a transient paramagnetic-like state exists when the pump fluence is above  $F_c$ , which recovers through a path distinctly different from the fast recovery for lower pump laser fluences. We note that the

different time scales observed in many magnetic spectroscopy experiments to date (3, 15) can be explained by depth averaging, where parts of the material near the surface undergo a transient magnetic phase transition with slow recovery dynamics, whereas layers deeper within the material exhibit faster recovery dynamics. This was confirmed by comparing an extensive set of fluence-dependent time-resolved ARPES and TMOKE data that show that the same critical behavior can explain the entire data set (26).

To further investigate the driving mechanisms for the observed critical phenomena during ultrafast laser-induced demagnetization, we repeated the same measurements for a sample temperature of 100 K using Tr-ARPES. Figure 4D plots the change of exchange splitting at a time delay of 2 ps as a function of pump fluence for sample temperatures of 300 and 100 K. The peak electron temperatures reached for those same sample temperatures are calculated using Eq. 1 and are shown in Fig. 4C. For a sample temperature of 100 K, the required critical fluence increases by  $\Delta F_T = 0.58$  mJ/cm<sup>2</sup> compared to room temperature (Fig. 4D). As shown in Fig. 4C, this offset can be precisely captured by Eq. 1 using the same transient heat capacity (inset of Fig. 4B), thus further validating the extracted value of this transient heat capacity. This result strongly suggests the following criterion for critical behavior in ultrafast demagnetization of Ni: whether or not the transient electron temperature exceeds the Curie temperature. Hence, in our work, the critical fluence corresponds to the fluence required to drive the transient electron temperature above the Curie temperature. We believe that the fact that the critical temperature observed in ultrafast demagnetization is very close to the Curie temperature under thermal equilibrium cannot be a simple coincidence but underscores the importance of the connection between the nonequilibrium physics and its equilibrium counterpart. Similar ideas were recently explored by studies on the ultrafast spin-density-wave transition in Cr (27). However, in that case, the spin-density-wave phase transition occurs immediately when the transient electron temperature reaches the critical point. In contrast, in our work, critical spin excitations occur within 20 fs, and the ferromagnetic-to-paramagnetic phase transition then happens on a longer time scale that is characteristic of the material. We believe that these mechanisms are broadly applicable to many different materials that undergo phase transitions at a critical temperature, for example, superconductors and charge-density-wave materials.

## DISCUSSION

Our results also shed light on the microscopic time evolution of electron spins during ultrafast demagnetization in Ni. The presence of critical behaviors in the electron temperature and heat capacity shows that, within 20 fs after excitation, the spin system in Ni has already absorbed sufficient energy to go through the ferromagnetic-to-paramagnetic

**Table 1. Fitting parameters for the electron and magnetic heat capacity under thermal equilibrium (25) and in the transient state.**

	$A$ (J/mol per K)	$A'$ (J/mol per K)	$\beta$ (J/mol per K)	$B$ (J/mol per K)	$B'$ (J/mol per K)	$T_c$ (K)	$\gamma$ (J/mol per K)
Equilibrium	$0.775 \pm 0.045$	$2.46 \pm 0.05$	$-0.0718 \pm 0.012$	$13.5 \pm 1.8$	$37.0 \pm 5.5$	$634 \pm 1$	$3.03 \pm 0.06$
Transient	0.775	2.46	-0.0718	$12.6 \pm 3.4$	$42.0 \pm 3.7$	$646 \pm 128$	$7.69 \pm 3.72$

phase transition, without yet exhibiting significant demagnetization. This time scale is much shorter than the time scale of demagnetization (TMOKE) and collapse of the exchange splitting (ARPES) ( $\sim 176$  fs). The very large difference between these two time scales indicates the importance of a highly nonequilibrium transient state before the sample reaches maximum demagnetization. The initial transferred energy must be stored in the spin system in the form of high-energy spin excitations, leaving the spin system in a nonequilibrium state. Then, this energy likely decays into low-energy magnons over time, leading to demagnetization of the sample in  $\sim 176$  fs. In this picture, the time scale and critical fluence of the demagnetization is intrinsic to the material itself and is determined by the Curie temperature, heat capacity, and exchange energy. This is strongly supported by the fact that the time constant of demagnetization in Ni ( $\sim 176$  fs) is independent of pump laser fluence, as shown by both the Tr-ARPES and Tr-TMOKE measurements (Fig. 2D). It has been suggested both experimentally and theoretically that the emission of low-energy magnons on a time scale of tens of femtoseconds could have significant contributions to ultrafast demagnetization in ferromagnetic materials (7, 17, 28–30). Finally, we note that our results cannot be explained by the models based on spin-flip scattering, because, in those models, the demagnetization of the material occurring in several hundred femtoseconds is driven by the gradual transfer of the energy from hot electrons to electron spins via spin-orbit and electron-phonon interactions (3, 5, 8, 15). Moreover, these mechanisms should give rise to a fluence-dependent demagnetization and recovery times.

Now, an important question remains—what is the mechanism that could lead to high-energy spin excitations during the first 20 fs? On this time scale, we believe that superdiffusive spin currents could be an important candidate, considering the significant difference between the lifetimes of the majority and minority electrons at  $\sim 0.2$  eV above  $E_F$  (10, 11), as well as the extremely short time scale of spin transport ( $\sim 1$  fs over  $\sim 1$ -nm distance). However, it has also been shown both experimentally (31, 32) and theoretically (16, 18, 33) that the spin mixing via spin-orbit coupling can happen in a very short time, which might also contribute.

Furthermore, another interesting finding is that, as evidenced by the critical behavior of  $\Delta E_{\text{ex}}$  in Fig. 4B, because the spin system recovers to the ground-state magnetization, two different recovery regimes exist, depending on the pump fluence. We note that this is the first time that such a critical behavior in the ultrafast decay and recovery time scales has been observed in ferromagnetic metals such as Ni. As noted above, the demagnetization and exchange-splitting collapse times are fluence-independent at  $\sim 176$  fs. However, when the pump fluence is lower than  $F_c$ , we find that the magnetization of the sample undergoes a fast recovery to the ferromagnetic phase with a time constant of  $\sim 500$  fs (Fig. 2A). This fast recovery might be explained by damping of magnons (the precession of the magnetic moment  $\mathbf{M}$ ) under the exchange field ( $\mathbf{H}_{\text{ex}}$ ). The typical damping time is given by  $\tau_{\text{damp}} = \frac{\hbar}{g\mu_B\mu_0|\mathbf{H}_{\text{ex}}|\alpha}$  using the Landau-Lifshitz-Gilbert equation (34, 35), where  $\mu_B$  is the Bohr magneton,  $g \approx 2$  is the Landé factor, and  $\alpha$  is the damping factor. Considering that  $\alpha \approx 0.065$  (36, 37) and  $|\mathbf{H}_{\text{ex}}| = 939$  T for Ni (38), we find  $\tau_{\text{damp}} \approx 580$  fs, which is in quantitative agreement with  $\tau_{\text{recover1}}$  observed in our experiments. On the other hand, when the pump fluence is above  $F_c$ , the sample evolves into a transient magnetic state with low magnetization and  $|\mathbf{H}_{\text{ex}}|$  is melted (see Fig. 1A). As a result, the magnetization must recover by coupling to phonons and the lattice, which occurs over much longer times.

In conclusion, by investigating ultrafast laser-induced demagnetization in Ni using fluence- and temperature-dependent ARPES, TMOKE, and EUV transient reflectivity measurements, we unambiguously show that critical phenomena govern the ultrafast demagnetization response. We find that although demagnetization and the collapse of the exchange splitting occur on the same fluence-independent time scale of  $\sim 176$  fs, sufficient energy for the transient magnetic phase transition has been transferred to the spin system already within  $\sim 20$  fs. Our results suggest the existence of a high-energy nonequilibrium transient magnetic state and that the transient electron temperature alone is responsible for crossing the spin electronic phase transition.

## MATERIALS AND METHODS

### Experimental setups

In the ARPES experiment, photoelectrons from the Ni(111) surface are mapped using 16-eV HHG probe pulses at near-normal incidence ( $5^\circ$ ) and collected by a momentum-resolved hemispherical analyzer. The output of a Ti:Sapphire laser amplifier system (KMLabs Dragon) is frequency doubled to 390 nm and used to generate high harmonics with  $\sim 160$ -meV energy resolution and well-separated (by  $\sim 6$  eV) harmonic orders that allow us to use the fifth harmonic ( $\sim 16$  eV) directly (39). For the TMOKE and EUV transient reflectivity experiments, the harmonics are driven directly with the 780-nm laser. Light near HHG orders 43 and 45, at photon energies of 65 and 68 eV, is used to probe the 3p absorption edge of Ni. For this purpose, the HHG probe beam is reflected from the sample at an angle of  $48^\circ$  from normal, spectrally dispersed by a grating, and recorded with a charge-coupled device (CCD) camera (9, 11, 30). The sample is fully magnetized in-plane by an electromagnet placed in the transverse geometry (see the Supplementary Materials for more details).

### Data analysis

In TMOKE, the sample magnetization is characterized by the change in reflected EUV intensity at the 3p absorption edge for opposite orientations of the initial in-plane magnetization vector. The TMOKE asymmetry ( $A_s$ ) is then calculated from

$$A_s = \frac{I_+ - I_-}{I_+ + I_-} \quad (2)$$

where  $I_+$  and  $I_-$  are the reflected EUV intensities for two magnetization directions (9, 40, 41). Details of data analysis of ARPES experiments are presented in detail in the Supplementary Materials.

The dynamics of TMOKE asymmetry ( $A_s$ ) and the change of the exchange splitting ( $\Delta E_{\text{ex}}$ ) can both be fit to

$$Y(t_d) = \begin{cases} Y_0 & (t_d < 0) \\ Y_0 + a e^{-t_d/\tau_{\text{demag}}} - b e^{-t_d/\tau_{\text{recover1}}} - (a - b) e^{-t_d/\tau_{\text{recover2}}} & (t_d \geq 0) \end{cases} \quad (3)$$

where  $Y$  represents either  $\Delta E_{\text{ex}}$  or  $A_s$ ,  $Y_0$  is the ground-state signal, and  $a$  and  $b$  are the amplitudes of the collapse and the first fast recovery of the signal, respectively.  $\tau_{\text{demag}}$ ,  $\tau_{\text{recover1}}$ , and  $\tau_{\text{recover2}}$  are the time constants of the collapse, fast recovery, and slow recovery of the signal, respectively.



## Model of electronic and magnetic heat capacity

The electronic and magnetic heat capacity  $C_e(T) + C_m(T)$  can be modeled with the following power-law function as it passes through the critical temperature ( $T_c$ ) (42)

$$C_e(t) + C_m(t) = \frac{A}{\beta} |t|^{-\beta} + B + \gamma t \quad (4)$$

where  $t \equiv \frac{T-T_c}{T_c}$  is the reduced temperature for  $T > T_c$ . We used the same function with primed parameters ( $A'$ ,  $B'$ ) for  $T < T_c$ . The parameters  $\beta$ ,  $\gamma$ , and  $T_c$  are kept identical on both sides of the phase transition. The electronic and magnetic heat capacities under thermal equilibrium conditions (25) can be fit to Eq. 4, allowing us to extract parameters  $A$ ,  $A'$ , and  $\beta$ , which determine the critical behavior of the heat capacities around  $T_c$ .

The contribution of the electron heat capacity alone can be estimated under the free-electron gas approximation  $C_e = \gamma T$  (see the Supplementary Materials) and gives rise to the modeled peak electron temperature using Eq. 1, as shown by the dashed line in Fig. 4A. We also noted that in Eq. 1, we neglected electron-phonon coupling and heat diffusion; however, these effects have negligible influence on our results in the first 20 fs, as shown in the Supplementary Materials.

## Statistical analysis

In both Tr-ARPES and Tr-TMOKE experiments, the data were collected with multiple pump-probe delay cycles to achieve a sufficient signal-to-noise ratio. The exchange splitting dynamics were analyzed by fitting the extracted photoemission spectra with multiple Voigt functions and defined as the energy difference between peaks of electrons with majority and minority spins (see the Supplementary Materials for more details). The error bars in Figs. 2A and 4 (B and D) were due to uncertainties in the fitting procedure. The transient electron temperature was obtained by fitting the photoemission intensity above  $E_F$  with Fermi-Dirac distribution, and the error bars in Figs. 3B and 4A were due to uncertainties in the fitting procedure, as well as the energy resolution (see the Supplementary Materials). The errors on the pump fluence were due to fluctuations of pump power and laser spot size. The error bars of Tr-TMOKE data in Fig. 2 (A and D) were defined by the SD of experimental data before pump excitation.

## SUPPLEMENTARY MATERIALS

Supplementary material for this article is available at <http://advances.sciencemag.org/cgi/content/full/4/3/eaap9744/DC1>

- section S1. Details of experimental setups.
- section S2. Dynamics of electron temperature.
- section S3. Dynamics of the electron population at 1.6 eV.
- section S4. Dynamics of exchange splitting.
- section S5. Temperature dependence of exchange splitting in static ARPES.
- section S6. Method for extracting TMOKE asymmetry dynamics from HHG spectra.
- section S7. Momentum dependence of TMOKE measurements.
- section S8. Transient electron and magnetic heat capacity.
- section S9. Effects of electron-phonon coupling and heat diffusion on Eq. 1.
- fig. S1. Experimental setup.
- fig. S2. Electron temperature fitting.
- fig. S3. Electron population dynamics.
- fig. S4. Analysis of exchange splitting.
- fig. S5. Global fitting of the exchange splitting dynamics.
- fig. S6. Collapse of exchange splitting at the Curie temperature.
- fig. S7. Momentum dependence of TMOKE measurements.

fig. S8. Electron and spin heat capacities.

fig. S9. Two-temperature model.

table S1. Material parameters used in TTM simulation.

References (43–50)

## REFERENCES AND NOTES

1. J. Stöhr, H. C. Siegmann, *Magnetism: From Fundamental to Nanoscale Dynamics* (Springer, 2006).
2. E. Beaupaire, J.-C. Merle, A. Daunois, J.-Y. Bigot, Ultrafast spin dynamics in nickel. *Phys. Rev. Lett.* **76**, 4250–4253 (1996).
3. B. Koopmans, G. Malinowski, F. Dalla Longa, D. Steiauf, M. Fähnle, T. Roth, M. Cinchetti, M. Aeschlimann, Explaining the paradoxical diversity of ultrafast laser-induced demagnetization. *Nat. Mater.* **9**, 259–265 (2009).
4. G. P. Zhang, W. Hübner, G. Lefkidis, Y. Bai, T. F. George, Paradigm of the time-resolved magneto-optical Kerr effect for femtosecond magnetism. *Nat. Phys.* **5**, 499–502 (2009).
5. M. Krauß, T. Roth, S. Alebrand, D. Steil, M. Cinchetti, M. Aeschlimann, H. Christian Schneider, Ultrafast demagnetization of ferromagnetic transition metals: The role of the Coulomb interaction. *Phys. Rev. B* **80**, 180407 (2009).
6. J.-Y. Bigot, M. Vomir, E. Beaupaire, Coherent ultrafast magnetism induced by femtosecond laser pulses. *Nat. Phys.* **5**, 515–520 (2009).
7. E. Carpenne, H. Hedayat, F. Boschini, C. Dallera, Ultrafast demagnetization of metals: Collapsed exchange versus collective excitations. *Phys. Rev. B* **91**, 174414 (2015).
8. B. Y. Mueller, A. Baral, S. Vollmar, M. Cinchetti, M. Aeschlimann, H. C. Schneider, B. Rethfeld, Feedback effect during ultrafast demagnetization dynamics in ferromagnets. *Phys. Rev. Lett.* **111**, 167204 (2013).
9. C. La-O-Vorakiat, E. Turgut, C. A. Teale, H. C. Kapteyn, M. M. Murnane, S. Mathias, M. Aeschlimann, C. M. Schneider, J. M. Shaw, H. T. Nembach, T. J. Silva, Ultrafast demagnetization measurements using extreme ultraviolet light: Comparison of electronic and magnetic contributions. *Phys. Rev. X* **2**, 011005 (2012).
10. M. Battiatto, K. Carva, P. M. Oppeneer, Superdiffusive spin transport as a mechanism of ultrafast demagnetization. *Phys. Rev. Lett.* **105**, 027203 (2010).
11. D. Rudolf, C. La-O-Vorakiat, M. Battiatto, R. Adam, J. M. Shaw, E. Turgut, P. Maldonado, S. Mathias, P. Grychtol, H. T. Nembach, T. J. Silva, M. Aeschlimann, H. C. Kapteyn, M. M. Murnane, C. M. Schneider, P. M. Oppeneer, Ultrafast magnetization enhancement in metallic multilayers driven by superdiffusive spin current. *Nat. Commun.* **3**, 1037 (2012).
12. B. Vodungbo, B. Tudou, J. Perron, R. Delaunay, L. Müller, M. H. Berntsen, G. Grübel, G. Malinowski, C. Weier, J. Gautier, G. Lambert, P. Zeitoun, C. Gutt, E. Jal, A. H. Reid, P. W. Granitzka, N. Jaouen, G. L. Dakovski, S. Moeller, M. P. Minitti, A. Mitra, S. Carron, B. Pfau, C. von Korff Schmising, M. Schneider, S. Eisebitt, J. Lüning, Indirect excitation of ultrafast demagnetization. *Sci. Rep.* **6**, 18970 (2016).
13. A. Eschenlohr, M. Battiatto, P. Maldonado, N. Pontius, T. Kachel, K. Holldack, R. Mitzner, A. Föhlisch, P. M. Oppeneer, C. Stamm, Ultrafast spin transport as key to femtosecond demagnetization. *Nat. Mater.* **12**, 332–336 (2013).
14. A. Rundquist, C. G. Durfee III, Z. Chang, C. Herne, S. Backus, M. M. Murnane, H. C. Kapteyn, Phase-matched generation of coherent soft x-rays. *Science* **280**, 1412–1415 (1998).
15. T. Roth, A. J. Schellekens, S. Alebrand, O. Schmitt, D. Steil, B. Koopmans, M. Cinchetti, M. Aeschlimann, Temperature dependence of laser-induced demagnetization in Ni: A key for identifying the underlying mechanism. *Phys. Rev. X* **2**, 021006 (2012).
16. W. Töws, G. M. Pastor, Many-body theory of ultrafast demagnetization and angular momentum transfer in ferromagnetic transition metals. *Phys. Rev. Lett.* **115**, 217204 (2015).
17. Y. Zhang, T.-H. Chuang, Kh. Zakeri, J. Kirschner, Relaxation time of terahertz magnons excited at ferromagnetic surfaces. *Phys. Rev. Lett.* **109**, 087203 (2012).
18. K. Krieger, J. K. Dewhurst, P. Elliott, S. Sharma, E. K. U. Gross, Laser-induced demagnetization at ultrashort time scales: Predictions of TDDFT. *J. Chem. Theory Comput.* **11**, 4870–4874 (2015).
19. D. L. Miller, M. W. Keller, J. M. Shaw, A. N. Chiamonti, R. R. Keller, Epitaxial (111) films of Cu, Ni, and  $\text{Cu}_2\text{Ni}_3$  on  $\alpha\text{-Al}_2\text{O}_3$  (0001) for graphene growth by chemical vapor deposition. *J. Appl. Phys.* **112**, 064317 (2012).
20. G. Salvatella, R. Gort, K. Bühlmann, S. Däster, A. Vaterlaus, Y. Acremann, Ultrafast demagnetization by hot electrons: Diffusion or super-diffusion? *Struct. Dyn.* **3**, 055101 (2016).
21. T. Greber, T. Kreutz, J. Osterwalder, Photoemission above the Fermi level: The top of the minority  $d$  band in nickel. *Phys. Rev. Lett.* **79**, 4465–4468 (1997).
22. H.-S. Rhie, H. A. Dürr, W. Eberhardt, Femtosecond electron and spin dynamics in Ni/W(110) films. *Phys. Rev. Lett.* **90**, 247201 (2003).
23. R. Knorren, K. H. Bennemann, R. Burgermeister, M. Aeschlimann, Dynamics of excited electrons in copper and ferromagnetic transition metals: Theory and experiment. *Phys. Rev. B* **61**, 9427–9440 (2000).
24. C. Chen, Z. Tao, A. Carr, P. Matyba, T. Szilvási, S. Emmerich, M. Piecuch, M. Keller, D. Zusin, S. Eich, M. Rollinger, W. You, S. Mathias, U. Thumm, M. Mavrikakis, M. Aeschlimann, P. M. Oppeneer, H. Kapteyn, M. Murnane, Distinguishing attosecond electron–electron

- scattering and screening in transition metals. *Proc. Natl. Acad. Sci. U.S.A.* **114**, E5300–E5307 (2017).
25. P. J. Meschter, J. W. Wright, C. R. Brooks, T. G. Kolliie, Physical contributions to the heat capacity of nickel. *J. Phys. Chem. Solids* **42**, 861–871 (1981).
  26. W. You, P. Tengdin, C. Chen, X. Shi, D. Zusin, Y. Zhang, C. Gentry, A. Blonsky, M. Keller, P. M. Oppeneer, H. Kapteyn, Z. Tao, M. Murnane, Correlating EUV TMOKE and ARPES measurements to understand the temporal and spatial length scales underlying ultrafast demagnetization in ferromagnets. <http://arxiv.org/abs/1712.07085> (2017).
  27. C. W. Nicholson, C. Monney, R. Carley, B. Frietsch, J. Bowlan, M. Weinelt, M. Wolf, Ultrafast spin density wave transition in chromium governed by thermalized electron gas. *Phys. Rev. Lett.* **117**, 136801 (2016).
  28. C. Illg, M. Haag, M. Fähnle, Ultrafast demagnetization after laser irradiation in transition metals: Ab initio calculations of the spin-flip electron-phonon scattering with reduced exchange splitting. *Phys. Rev. B* **88**, 214404 (2013).
  29. A. B. Schmidt, M. Pickel, M. Donath, P. Buczek, A. Ernst, V. P. Zhukov, P. M. Echenique, L. M. Sandratskii, E. V. Chulkov, M. Weinelt, Ultrafast magnon generation in an Fe film on Cu(100). *Phys. Rev. Lett.* **105**, 197401 (2010).
  30. E. Turgut, D. Zusin, D. Legut, K. Carva, R. Knut, J. M. Shaw, C. Chen, Z. Tao, H. T. Nembach, T. J. Silva, S. Mathias, M. Aeschlimann, P. M. Oppeneer, H. C. Kapteyn, M. M. Murnane, P. Grychtol, Stoner versus Heisenberg: Ultrafast exchange reduction and magnon generation during laser-induced demagnetization. *Phys. Rev. B* **94**, 220408 (2016).
  31. C. Stamm, T. Kachel, N. Pontius, R. Mitzner, T. Quast, K. Holldack, S. Khan, C. Lupulescu, E. F. Aziz, M. Wietstruk, H. A. Dürr, W. Eberhardt, Femtosecond modification of electron localization and transfer of angular momentum in nickel. *Nat. Mater.* **6**, 740–743 (2007).
  32. C. Stamm, M. Pontius, T. Kachel, M. Wietstruk, H. A. Dürr, Femtosecond x-ray absorption spectroscopy of spin and orbital angular momentum in photoexcited Ni films during ultrafast demagnetization. *Phys. Rev. B* **81**, 104425 (2010).
  33. G. P. Zhang, W. Hübner, Laser-induced ultrafast demagnetization in ferromagnetic metals. *Phys. Rev. Lett.* **85**, 3025–3028 (2000).
  34. T. L. Gilbert, Classics in magnetism: a phenomenological theory of damping in ferromagnetic materials. *IEEE Trans. Magn.* **40**, 3443–3449 (2004).
  35. B. Koopmans, J. J. M. Ruigrok, F. Dalla Longa, W. J. M. de Jonge, Unifying ultrafast magnetization dynamics. *Phys. Rev. Lett.* **95**, 267207 (2005).
  36. J. Walowski, M. Djordjevic Kaufmann, B. Lenk, C. Hamann, J. McCord, M. Münzenberg, Intrinsic and non-local Gilbert damping in polycrystalline nickel studied by Ti:Sapphire laser fs spectroscopy. *J. Phys. D Appl. Phys.* **41**, 164016 (2008).
  37. M. Oogane, T. Wakitani, S. Yakata, R. Yilgin, Y. Ando, A. Sakuma, T. Miyazaki, Magnetic damping in ferromagnetic thin films. *Jpn. J. Appl. Phys.* **45**, 3889–3891 (2006).
  38. R. M. White, *Quantum Theory of Magnetism* (Springer-Verlag, 2007).
  39. S. Eich, A. Stange, A. V. Carr, J. Urbancic, T. Popmintchev, M. Wiesenmayer, K. Jansen, A. Ruffing, S. Jakobs, T. Rohwer, S. Hellmann, C. Chen, P. Matyba, L. Kipp, K. Rossnagel, M. Bauer, M. M. Murnane, H. C. Kapteyn, S. Mathias, M. Aeschlimann, Time- and angle-resolved photoemission spectroscopy with optimized high-harmonic pulses using frequency-doubled Ti:Sapphire lasers. *J. Electron Spectrosc. Relat. Phenom.* **195**, 231–236 (2014).
  40. S. Mathias, C. La-O-Vorakiat, P. Grychtol, P. Granitzka, E. Turgut, J. M. Shaw, R. Adam, H. T. Nembach, M. E. Siemens, S. Eich, C. M. Schneider, T. J. Silva, M. Aeschlimann, M. M. Murnane, H. C. Kapteyn, Probing the timescale of the exchange interaction in a ferromagnetic alloy. *Proc. Natl. Acad. Sci. U.S.A.* **109**, 4792–4797 (2012).
  41. C. La-O-Vorakiat, M. Siemens, M. M. Murnane, H. C. Kapteyn, S. Mathias, M. Aeschlimann, P. Grychtol, R. Adam, C. M. Schneider, J. M. Shaw, H. Nembach, T. J. Silva, Ultrafast demagnetization dynamics at the *M* edges of magnetic elements observed using a tabletop high-harmonic soft x-ray source. *Phys. Rev. Lett.* **103**, 257402 (2009).
  42. A. Kornblit, G. Ahlers, Heat capacity of EuO near the Curie temperature. *Phys. Rev. B* **11**, 2678–2688 (1975).
  43. P. B. Johnson, R. W. Christy, Optical constants of transition metals: Ti, V, Cr, Mn, Fe, Co, Ni, and Pd. *Phys. Rev. B* **9**, 5056–5070 (1974).
  44. D. A. Shirley, High-resolution x-ray photoemission spectrum of the valence bands of gold. *Phys. Rev. B* **5**, 4709–4714 (1972).
  45. R. Carley, K. Döbrich, B. Frietsch, C. Gahl, M. Teichmann, O. Schwarzkopf, P. Wernet, M. Weinelt, Femtosecond laser excitation drives ferromagnetic gadolinium out of magnetic equilibrium. *Phys. Rev. Lett.* **109**, 057401 (2012).
  46. B. Y. Mueller, T. Roth, M. Cinchetti, M. Aeschlimann, B. Rethfeld, Driving force of ultrafast magnetization dynamics. *New J. Phys.* **13**, 123010 (2011).
  47. V. Korenman, R. E. Prange, Temperature dependence of the angle-resolved photoemission in itinerant-electron ferromagnets. *Phys. Rev. Lett.* **44**, 1291–1294 (1980).
  48. J. K. Chen, D. Y. Tzou, J. E. Beraun, A semiclassical two-temperature model for ultrafast laser heating. *Int. J. Heat Mass Transfer* **49**, 307–316 (2006).
  49. A. M. Chen, A. M. Chen, H. F. Xu, Y. F. Jiang, L. Z. Sui, D. J. Ding, H. Liu, M. X. Jin, Modeling of femtosecond laser damage threshold on the two-layer metal films. *Appl. Surf. Sci.* **257**, 1678–1683 (2010).
  50. Z. Lin, L. V. Zhigilei, V. Celli, Electron-phonon coupling and electron heat capacity of metals under conditions of strong electron-phonon nonequilibrium. *Phys. Rev. B* **77**, 075133 (2008).

**Acknowledgments:** We thank G. Cao and L. Miaja-Avila for helpful discussions. **Funding:** The experimental measurements were performed at JILA. M.M.M. and H.C.K. gratefully acknowledge support for the ARPES measurements from the NSF through the JILA Physics Frontiers Center PHY-1125844 and a Gordon and Betty Moore Foundation EPIQS Award GBMF4538. They also thank the Department of Energy Office of Basic Energy Sciences X-Ray Scattering Program Award DE-SC0002002 for the magnetic TMOKE spectroscopy measurements performed for this work. P.M.O. acknowledges support from the Swedish Research Council (VR), the Wallenberg Foundation (grant no. 2015.0060) and European Union Horizon 2020 grant no. 737709 “FEMTOTERABYTE.” **Author contributions:** M.M.M., H.C.K., Z.T., P.T., and C.C. conceived the project. P.T., W.Y., C.C., X.S., D.Z., Y.Z., C.G., A.B., and Z.T. conducted the experiments. P.T., W.Y., C.C., X.S., and Z.T. analyzed the data. M.K. prepared the sample. P.M.O. provided theory support. P.T., W.Y., X.S., P.M.O., Z.T., and M.M.M. wrote the manuscript with inputs from all other authors. **Competing interests:** H.C.K. and M.M.M. have a financial interest in a laser company, KMLabs, that produces the lasers and HHG sources used in this work. H.C.K. is partially employed by KMLabs. The authors declare that they have no other competing interests. **Data and materials availability:** All data needed to evaluate the conclusions in the paper are present in the paper and/or the Supplementary Materials. Additional data related to this paper may be requested from the authors.

Submitted 15 September 2017

Accepted 31 January 2018

Published 2 March 2018

10.1126/sciadv.aap9744

**Citation:** P. Tengdin, W. You, C. Chen, X. Shi, D. Zusin, Y. Zhang, C. Gentry, A. Blonsky, M. Keller, P. M. Oppeneer, H. C. Kapteyn, Z. Tao, M. M. Murnane, Critical behavior within 20 fs drives the out-of-equilibrium laser-induced magnetic phase transition in nickel. *Sci. Adv.* **4**, eaap9744 (2018).



## Critical behavior within 20 fs drives the out-of-equilibrium laser-induced magnetic phase transition in nickel

Phoebe TengdinWenjing YouCong ChenXun ShiDmitriy ZusinYingchao ZhangChristian GentryAdam BlonskyMark KellerPeter M. OppeneerHenry C. KapteynZhensheng TaoMargaret M. Murnane

*Sci. Adv.*, 4 (3), eaap9744. • DOI: 10.1126/sciadv.aap9744

### View the article online

<https://www.science.org/doi/10.1126/sciadv.aap9744>

### Permissions

<https://www.science.org/help/reprints-and-permissions>